PCCP

Accepted Manuscript

This is an *Accepted Manuscript*, which has been through the Royal Society of Chemistry peer review process and has been accepted for publication.

Accepted Manuscripts are published online shortly after acceptance, before technical editing, formatting and proof reading. Using this free service, authors can make their results available to the community, in citable form, before we publish the edited article. We will replace this *Accepted Manuscript* with the edited and formatted *Advance Article* as soon as it is available.

You can find more information about *Accepted Manuscripts* in the Information for Authors.

Please note that technical editing may introduce minor changes to the text and/or graphics, which may alter content. The journal's standard Terms & Conditions and the Ethical guidelines still apply. In no event shall the Royal Society of Chemistry be held responsible for any errors or omissions in this *Accepted Manuscript* or any consequences arising from the use of any information it contains.

ROYAL SOCIETY OF CHEMISTRY

www.rsc.org/pccp

$LiNi_{0.5}Mn_{1.5}O_4$ High-Voltage Cathode Coated with $Li_4Ti_5O_{12}$: A Hard X-ray Photoelectron Spectroscopy (HAXPES) Study

Malte Sachs[a], Michael Gellert[a], Min Chen[a], Hans-Jörg Drescher[a], Stefan Renato Kachel[a], Han Zhou[a], Malte Zugermeier[a], Mihaela Gorgoi[b], Bernhard Roling[a] and J. Michael Gottfried[a]*

[a]*Fachbereich Chemie, Philipps-Universität Marburg, Hans-Meerwein-Straße 4, 35032 Marburg, Germany*

[b]*Helmholtz Zentrum Berlin für Materialien und Energie GmbH, Albert-Einstein-Straße 15, 12489 Berlin, Germany*

Corresponding author address:
Prof. Dr. Michael Gottfried
Philipps - Universität Marburg, Fachbereich Chemie
Hans-Meerwein-Straße 4, 35032 Marburg, Germany
michael.gottfried@chemie.uni-marburg.de
+49 6421 28 22541 (Tel) +49 6421 28 22542 (Fax)

Physical Chemistry Chemical Physics Accepted Manuscript

Abstract

A $Li_4Ti_5O_{12}$ (LTO) film was coated as buffer layer onto a $LiNi_{0.5}Mn_{1.5}O_4$ (LNMO) high-voltage cathode, and after cycling of the cathode in a battery electrolyte, the LTO film was investigated by means of synchrotron radiation based Hard X-ray Photoelectron Spectroscopy (HAXPES). By tuning the photon energy between 2 keV and 6 keV, we obtained non-destructive depth profiles of the coating material with probing depths ranging from 6 nm to 20 nm. The coating was found to be covered by a few nanometers thin surface layer resulting from electrolyte decomposition. This layer consisted predominantly of organic polymers as well as metal fluorides and fluorophosphates. A positive influence of the $Li_4Ti_5O_{12}$ coating with regard to the size and stability of the surface layer was found. The coating itself consisted of a uniform mixture of Li(I), Ti(IV), Ni(II) and Mn(IV) oxides that most likely adopted a spinel structure by forming a solid solution of the two spinels $LiNi_{0.5}Mn_{1.5}O_4$ and $Li_4Ti_5O_{12}$ with Li, Mn, Ni and Ti cations mixing on the spinel octahedral sites. The diffusion of Ni and Mn ions into the $Li_4Ti_5O_{12}$ lattice occurred during the heat treatment when preparing the cathode. The doping of $Li_4Ti_5O_{12}$ with the open d-shell ions Ni^{2+} (d^8) and Mn^{4+} (d^3) should increase the electronic conductivity of the coating significantly, as was found in previous studies. The complex signal structure of the Ti 2p, Ni 2p and Mn 2p core levels provides insight into the chemical nature of the transition metal ions.

Physical Chemistry Chemical Physics Accepted Manuscript

1. Introduction

Hard X-ray photoelectron spectroscopy (HAXPES) experienced a rapid development in the recent years. Many third-generation synchrotron radiation sources offer opportunities for high-resolution photoelectron spectroscopy in a kinetic energy (KE) range up to 10 – 15 keV, enabling non-destructive, bulk-sensitive XPS measurements with considerably increased information depth of several tens of nanometers.[1,2] Varying the inelastic mean free path (IMFP) by tuning the kinetic energy of the photoelectrons provides a tool for depth-profiling the chemical composition of buried interfaces.

An increasing number of studies of electrodes and electrode/electrolyte interfaces benefits from this technique.[3–7] The non-destructive depth-profiling approach is advantageous over destructive sputtering techniques, because the latter can change the chemical composition of the interface due to elements-specific sputter rates.[8,9] To our knowledge, the present work is the first HAXPES study of the high-voltage cathode material $LiNi_{0.5}Mn_{1.5}O_4$ (LNMO) for lithium-ion batteries. LNMO crystallizes in a spinel structure allowing for three-dimensional Li^+ ion transport and exhibits a redox potential of 4.7 V vs. Li^+/Li.[10] In typical battery electrolytes composed of organic carbonates and $LiPF_6$, LNMO suffers from complex surface reactions, which limit the chemical stability and electrochemical capacity.[11–17] It was shown that the application of buffer layers can help to protect the cathode material from the electrolyte and to improve the Coulombic efficiency and long-term stability.[18–24] A recent study on a model system consisting of thin-film LNMO cathodes covered with $Li_4Ti_5O_{12}$ (LTO) revealed unexpectedly low impedances.[25] In particular, a high impedance contribution expected for the LTO layer, which is known to exhibit a low ionic and electronic conductivity, was not detected. Time-of-flight secondary ion mass-spectroscopy (ToF-SIMS) indicated the presence of a solid electrolyte interphase (SEI) layer on the surface of the LTO coating as well as cross-diffusion of nickel and manganese ions from the LNMO layer into the LTO layer. In the light of these findings, more detailed information about the chemical composition of these layers would be highly beneficial. In the present study, we investigated the chemical composition of the SEI layer and of the LTO coating using HAXPES in an energy range of 2 – 6 keV. The tunable photon energy allows us to obtain non-destructive depth profiles for probing depths in the range of approximately 6 – 20 nm.

2. Experimental details

2.1. Sample preparation and electrochemical characterization

The thin-film cathode was prepared via a multi-step sol-gel assisted spin-coating procedure using a polished gold substrate. The detailed procedure was described elsewhere.[25] Briefly, the LNMO precursor sol was spin-coated on top of the substrate and allowed to dry. The coating and drying steps were repeated several times, until the desired LNMO layer thickness was achieved. Before the

Physical Chemistry Chemical Physics Accepted Manuscript

LTO layer was coated the LNMO layer, the LNMO layer was heated to 800 °C for 60 min in order to form a crystalline phase with spinel structure. The LTO precursor sol was then spin-coated on top of the Au/LNMO layer structure and dried. The spin-coating and drying step were repeated three times. Subsequently, the LTO/LNMO/Au layer structure was heated to 700 °C for 60 min to form crystalline LTO. The final projected layer structure is illustrated in Figure 1.

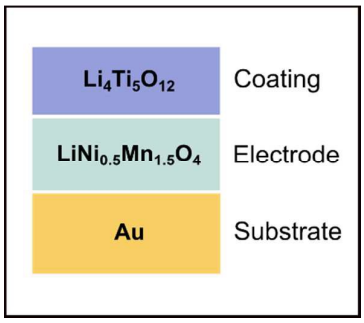

Figure 1. Idealized layer structure of the LTO-covered LNMO cathode after spin coating.

For the electrochemical measurements, a commercial cell TSC battery expanded (rhd instruments) was used. For galvanostatic charging and discharging experiments, a LNMO/LTO cathode was cycled several times in a half-cell configuration LNMO/LTO/liquid electrolyte/lithium by applying a current density of 50 µA/cm² in a potential range between 3.5 V and 4.9 V vs. (Li^+/Li) (Multi-Autolab, Metrohm Autolab B.V.). As liquid electrolyte, a 1M solution of $LiPF_6$ in EC/DMC (1:1) was used (LP30, Merck).

For the HAXPES measurements, a fresh LNMO/LTO cathode was first characterized by means of three consecutive cyclic voltammograms with a scanning speed of 1 mV/s and was subsequently charged and discharged once by applying a current density of 50 µA/cm² in a potential range between 3.5 V and 4.9 V vs. (Li^+/Li). After discharging to 3.5 V, the cell was disassembled and the cathode was rinsed with dimethyl carbonate.

2.2. HAXPES measurement procedure

For this experiment, Hard X-ray Photoemission Spectroscopy (HAXPES) in the photon energy range of 2 to 6 keV was used. The measurements were performed at the KMC-1 beamline of the synchrotron radiation facility BESSY II (Helmholtz-Zentrum für Materialien und Energie, Berlin, Germany) using the HIKE end-station with a Scienta R4000 hemispherical electron energy analyzer. The general properties of this setup were described elsewhere.[26,27] The spot size of the photon beam was approximately 0.3 x 0.4 mm^2. Typical photon fluxes were in the order of 10^{11} to 10^{12} photons/s over the entire energy range.

Physical Chemistry Chemical Physics Accepted Manuscript

The depth profile of the sample was obtained by stepwise increasing the photon energy. As the binding energy of a photoelectron line stays constant, the kinetic energy of the photoelectrons increases with increasing photon energy, enhancing the inelastic mean free path (IMFP) of the electrons. The tuning of the photoelectron IMFP allows to achieve different probing depths resulting in a depth profile of the sample. Five photon energies were used in steps of 1 keV starting with a photon energy of 2 keV.

For each photon energy a complete spectrum was collected in a binding energy range from zero to 1 keV. The measurements were carried out in Constant Analyzer Energy (CAE) mode with a pass energy of 200 eV. The data acquisition was performed in normal emission of the electrons and grazing incidence of the photon beam. To exclude beam damage effects, the sample was shifted to a new position after each measurement.

2.3. HAXPES data treatment

The binding energy scale was calibrated to the Au $4f_{7/2}$ photoelectron line of a reference gold sample. The intensities of the survey spectra were corrected with respect to the spectrometer transmission function *T*(KE), which describes the efficiency of the collection lens, energy analyzer and detector to detect photoelectrons in dependence on their kinetic energy.[28]

A standard Shirley background was used for signal deconvolution (fitting) of selected core level spectra. The fitting procedure was performed with *XPStools*[29], a custom-developed program package, implemented in the data analysis software IgorPro (Wavemetrics) using asymmetric Pseudo-Voigt functions with Lorentzian (X%) and Gaussian (100-X%) peak shapes. The best mixture of Gaussian-Lorentzian components GL(X%) is dependent on the instrument resolution and the natural line width of the specific core hole. The ratio was adjusted individually for each core level spectrum. The ratios are in a range of GL(0%) to GL(20%), because of a predominant instrumental Gaussian broadening. An exception is the treatment of the Ti 2p photoelectron lines that can only be fitted successfully with a higher amount of Lorentzian contribution.

The O 1s, F 1s, and C 1s spectra were fitted using the minimum number of peaks possible to represent the spectral shapes. Peak widths were set equal within the fit of a particular core level spectrum, as the instrumental Gaussian peak broadening is independent of the chemical species and the Lorentzian lifetime broadening should be similar for different chemical species in a first approximation. The relative peak positions were fixed to ±0.1 eV in corresponding spectra of different excitation energy. These slight variations were allowed to account for noise and scatter of the data points.

In the case of the O 1s, F 1s, and C 1s spectra, each fitting function should ideally represent a specific chemical species, which is characterized by its binding energy. However, because of the large number

Physical Chemistry Chemical Physics Accepted Manuscript

of possible reactions involved in an electrochemical experiment, the exact number of species that form the spectral shape is not known. The fitting functions that are applied here are an approximation of the exact number of species present. Therefore, they do not describe specific chemical species, but groups of species with a similar chemical shift.

The transition metal (TM) photoemission signals Ni 2p, Mn 2p or Ti 2p display complex peak shapes. They arise from various processes that can accompany the primary photoemission, including shake-up or plasmon loss structures and multiplet splitting, which make a multicomponent fit necessary, even if only a single chemical species is present. To obtain quantitative information about the sample composition from a spectrum that contains contributions from several chemical species requires accurate fitting models for each of the spectral components. Since such models are not always available, the focus of this paper was on the determination of the predominant chemical species. The complex peak shapes of transition metal photoelectron spectra can be used as fingerprints of chemical state of the species. In particular, the chemical state can be determined by investigating characteristic spectral features, e.g., the energy separation between the main photoelectron line and a specific satellite signal. Binding energies of single peak maxima are often not characteristic and should not be used alone to identify the chemical state of the TM ion.[30]

The analysis of the chemical state was mainly performed with the metal 2p photoelectron lines. The starting point of the analysis was the assignment of the $2p_{3/2}$ and $2p_{1/2}$ spin-orbit components and the identification of additional satellite signals. The spectral features used to assign the chemical state were taken from literature. The determined chemical state was the basis for the selection of an appropriate fitting model. In the literature, fitting models are often only given for the more intense $2p_{3/2}$ signals. Thus, only the $2p_{3/2}$ signals were used to confirm the chemical states by applying the appropriate fitting models to it. If necessary, these fitting models were modified empirically. The $2p_{1/2}$ peaks and additional satellite signals were fitted empirically to obtain the total intensity of the core level spectrum for the performed elemental composition analysis.

The probing depth d_p was defined as three times the IMFP $\lambda(\mathrm{KE})$ of the photoelectrons in the substrate multiplied with the sine of the electron take off angle versus the sample surface θ:

$$d_p = 3 \cdot \lambda(\mathrm{KE}) \cdot \sin\theta \quad (1)$$

Since the spectra were taken in normal emission here θ is 90°. IMFPs for TiO_2[31] were used to approximate the bulk IMFP and the probing depth.

Analysis of the elemental composition was performed based on the intensity area *A* of the curve fits. The signal depends in a first approximation on the concentration of the species in the sample, the probability of electron emission from a particular core level described by the cross section σ and the probing region dependent on the kinetic energy of the photoelectrons characterized with the IMFP

Physical Chemistry Chemical Physics Accepted Manuscript

λ(KE). The relative intensity $I_{j,h\nu}$ of a chemical species j measured at a photon energy $h\nu$ is then estimated with following equation:

$$I_{j,h\nu} = \frac{A_{j,h\nu}/[\sigma_{j,h\nu} \cdot \lambda(\mathrm{KE})_j]}{\sum_i A_{i,h\nu}/[\sigma_{i,h\nu} \cdot \lambda(\mathrm{KE})_i]} \quad (2)$$

in which the sum runs over all chemical species used for the elemental composition analysis. The relative intensities of titanium were calculated by averaging over the Ti 2p and Ti 2s spectra to compensate for uncertainties of the background determination. Scofield cross sections[32] were used for the σ values. The relative intensities were grouped to contributions from the bulk material and from the surface layer.

The sum of the relative bulk intensities $I_{\mathrm{bulk},h\nu}$ was used to estimate the thickness of the surface layer. The surface layer attenuates the bulk intensities to a certain amount that can be described by Beer's law:

$$I_{\mathrm{bulk},h\nu} = \mathrm{e}^{-\frac{d}{\lambda(\mathrm{KE})\,sin\theta}} \quad (3)$$

The quantity d is the thickness of the surface layer, $\lambda(\mathrm{KE})$ is the IMFP and θ the electron take off angle versus the sample surface. For $d \gg \lambda$ the relative bulk intensity should approach zero as the bulk electrons cannot cross the surface layer to reach the detector. Increasing the IMFP of the photoelectrons allows to detect more bulk electrons, which enlarges the relative bulk intensity.

The surface layer thickness d was calculated as the slope of the line of best fit for a plot of $\ln I_{\mathrm{bulk},h\nu}$ vs. $1/\lambda$. Polyethylene IMFP values from the *NIST Electron Inelastic-Mean-Free-Path Database*[33] were used to approximate the IMFP in the surface layer in line with previous work[6], as the surface layer consists predominantly of organic polymers formed by decomposition of the electrolyte. An average IMFP was estimated for the bulk photoelectrons by taking the mean value of their kinetic energies.

The bulk composition of the coating, $Ti_xNi_yMn_zO_4$, is calculated in relation to the relative intensity of the O 1s bulk oxide signal $I_{\mathrm{bulk,O1s}}$ using the intensities defined in Equation 2, e.g.:

$$x = \frac{I_{\mathrm{Ti}}}{I_{\mathrm{bulk,O1s}}} \cdot 4 \quad (4)$$

To investigate the dependency of the bulk composition on the applied background correction method, the intensity area of the Ni 2p, Mn 2p, Ti 2s, Ti 2p and O 1s spectra was additionally determined using a Tougaard background with the universal loss function and the energy loss parameter $C = 1643\ \mathrm{eV}^2$.[34] The background correction was applied in an area up to 40 eV above the main peak binding energy. The intensity area was obtained by numerical integration of the

Physical Chemistry Chemical Physics Accepted Manuscript

background corrected spectra. In the case of the O 1s spectra, the determined intensity area had to be corrected by the fraction of the intensity of the surface species, which was obtained by the fitting procedure discussed above. The relative intensities and the bulk composition were calculated using Equations 2 and 4.

3. Results and discussion

3.1 Electrochemical analysis

The LNMO/LTO/LP30/Li cell was charged galvanostatically and was discharged at a current density of 50 µA cm^{-2}. A selection of charge/discharge curves are shown in Fig. 2a. All curves exhibit two plateaus around 4.7 V vs. Li^+/Li, corresponding to the oxidation/reduction of the redox couples $Ni^{(2+/3+)}$ and $Ni^{(3+/4+)}$. Also present is an additional, less extended plateau around 4.0 V vs. (Li^+/Li), which is associated with the oxidation/reduction of $Mn^{(3+/4+)}$.

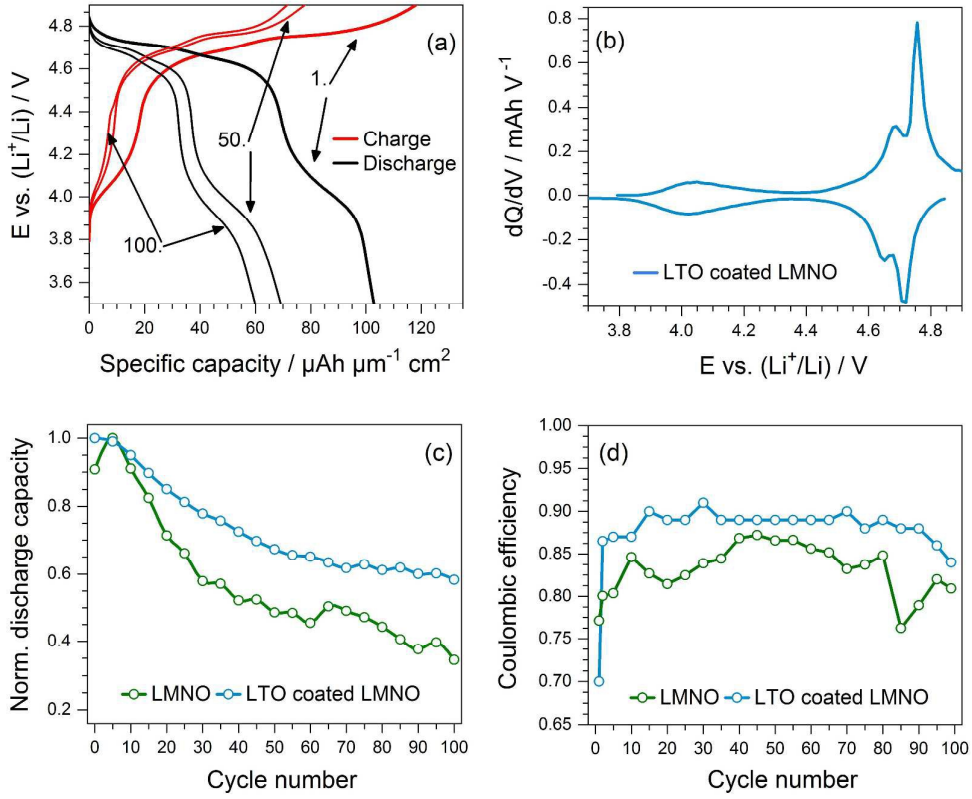

Figure 2. Electrochemical analysis of LTO coated LNMO cathodes. (a) Voltage profiles during galvanostatic charge/discharge, (b) a derivative plot dQ/dV, (c) normalized discharge capacity versus cycle number, and (d) Coulombic efficiency versus cycle number, for a coated and an uncoated LNMO cathode.

Physical Chemistry Chemical Physics Accepted Manuscript

The presence of Mn^{3+} becomes also more evident in the dQ/dV-plot in Fig. 2b. This is most likely due to an incomplete substitution of manganese ions in the spinel 16d sites with Ni^{2+}. Earlier studies[25] already indicated that the nickel deficiency is a result of cross-diffusion of Ni^{2+} from LNMO into the LTO coating, which is confirmed by characterizing the chemical composition of the LTO layer with HAXPES, see Section 3.4. In addition, the initial specific capacity is much higher than the theoretical capacity of uncoated LNMO (65.5 µAh μm^{-1} cm^{-2})[11], which is most likely a result of the diffusion of Mn and Ni into the LTO layer.

The effect of the LTO coating on the chemical stability in contact to liquid electrolyte was investigated by comparing the charge/discharge measurements to the ones conducted with an uncoated LNMO film. The LTO-coated sample showed an improved stability over time (Figure 2c), while the uncoated cathode retained only 35% of the maximum capacity after 100 cycles, the LTO coated sample retained nearly 60% of its initial capacity.

The Coulombic efficiency of the uncoated sample displayed in Figure 2d was in the range of 75% to 87%, which is comparable to results reported by Arrebola *et al*.[35] The LTO-coated sample showed more constant Coulombic efficiencies around 90 % (except for the first cycle). Taking into account both the enhanced capacity retention and the improved Coulombic efficiency, it can be concluded that the coating helps protecting the cathode material and the electrolyte from degradation. Nevertheless, at least 10% of the charge is available for parasitic side reactions, such as SEI formation at the interface of LTO/liquid electrolyte, which was also investigated by HAXPES analysis, as will be described in Section 3.3.

3.2. Survey spectra and depth profile

Figure 3 displays the survey HAXPES spectra of the LTO coated LNMO thin-film cathode (electrolyte: 1M $LiPF_6$ in EC/DMC 1:1) in its discharged state with the nominal composition $LiNi_{0.5}Mn_{1.5}O_4$ after conducting three cyclic voltammograms and a single charge and discharge cycle between 3.5 V und 4.9 V with a current density of 50 µA/cm². The spectral features can principally be assigned either to components originating from the electrode material (titanium, manganese, nickel and oxygen) or from electrolyte decomposition products (carbon, fluorine, oxygen) forming a surface layer on-top of the electrode. A detailed peak fitting analysis was performed with the highlighted elemental signals in Figure 3. It has to be emphasized that phosphorus and lithium signals were excluded from the analysis because of their low intensities.

Physical Chemistry Chemical Physics Accepted Manuscript

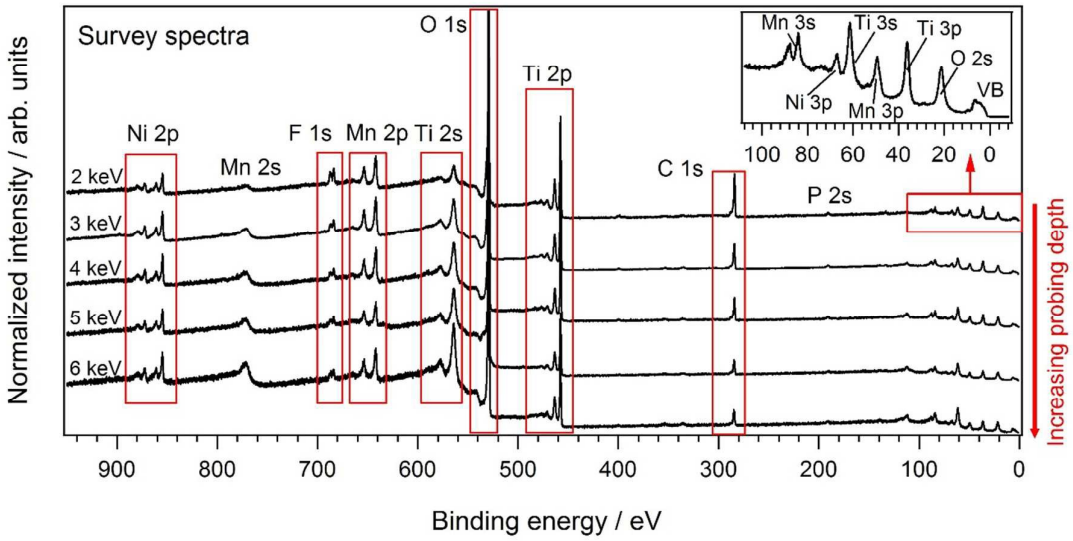

Figure 3. HAXPES survey spectra of the LTO-coated LNMO thin-film cathode with assignment of the spectral features to elemental core levels, for photon energies from 2 to 6 keV as indicated. Each spectrum was normalized by its total intensity area. The red boxes mark the regions used in further analysis.

Figure 4 displays the depth profile for the LTO coated LNMO thin-film cathode obtained by quantitative analysis of the data in Figure 3 as described in Section 2.3. The probing depth for a specific photon energy was estimated using Equation 1 by three times the average IMFP of the photoelectrons of all core levels used. The IMFP is dependent on the kinetic energy (KE) of the photoelectrons. Thus, the probing depth is not uniform for a given photon energy as the KE of the photoelectrons varies with the binding energies of the core levels. Especially the IMFP of high binding energy core levels such as Ni 2p compared with low binding energy core levels like C 1s should be quite different. However, in the high KE regime of HAXPES with IMFPs in the nanometer scale the difference between the individual IMFPs of the core levels fall below the error (about 20 %)[33] for estimating the IMFP itself by using approximated values. Even at a photon energy of 2 keV the individual IMFPs are in this range of error, which justifies the averaging. The chemical species were assigned to either components of the bulk electrode coating material or components of the surface layer. The surface layer attenuates the bulk intensities to a certain amount as was discussed in Section 2.3. The sum of the bulk intensities increase with increasing probing depth following an exponential trend as expected on the basis of Equation 3.

Physical Chemistry Chemical Physics Accepted Manuscript

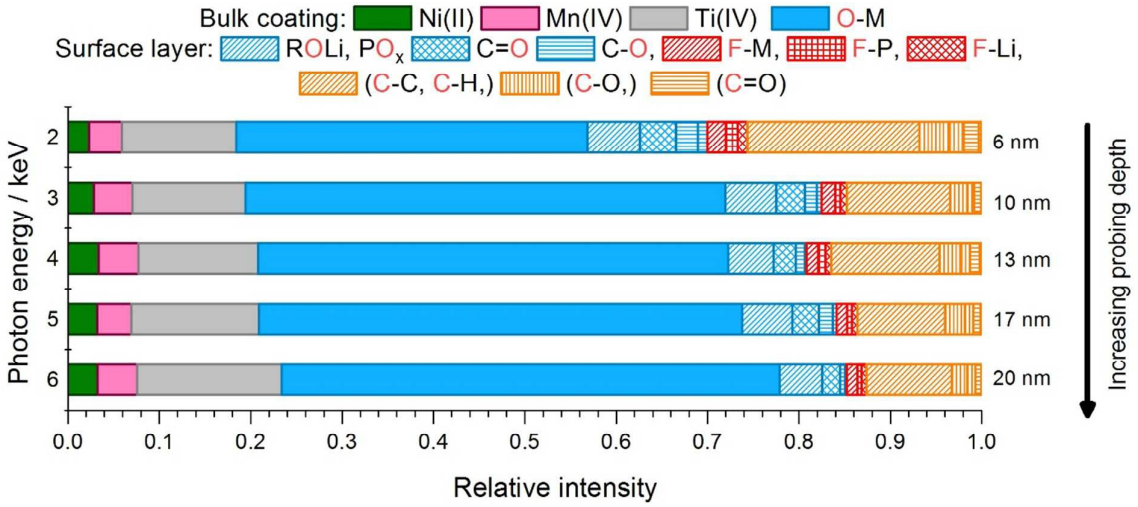

Figure 4. Near-surface depth profile of the LTO coated LNMO thin-film cathode. Relative intensities according to the curve fits of the core level spectra, grouped into contributions of the bulk coating and the surface layer. The predominant oxidation state of the metal ions is indicated. The average probing depth is specified on the right side of the graph. Increasing probing depth is indicated with an arrow.

3.3. Composition of the surface layer

The LTO coating is covered by a surface layer that consists mostly of organic polymers (90 %) and minority species, such as metal fluorides and fluorophosphates (10 %). The chemical composition was determined by analyzing the C 1s, O 1s and F 1s core level spectra (Figure 5). In case of the C 1s and O 1s spectra, the spectral shape is difficult to deconvolute into contributions from distinct chemical species, because the sample contains most likely a large number of C and O species with slightly different binding energies. In the O 1s signal, the intense main feature at 529.4 eV is attributed to the metal oxides of the bulk coating. Less intense contributions in the BE range from 530.5 eV to 533.4 eV can be assigned to various species that have previously been reported as typical decomposition products of the electrolyte (see Section 2.1): Poly(ethers), poly(carbonates), lithium alkoxides and carbonates.[9,36] The spectral features of the C 1s spectrum support these assignments: For example, the C 1s peak at 285.8 eV and the O 1s peak at 531.4 eV can be associated with poly(ethylene oxide) (PEO)[37], which is formed by direct polymerization of ethylene carbonate (EC) via poly(ethylene carbonate) (PEC):[14,16,38]

$$\mathrm{EC} \xrightarrow{\mathrm{PF_5}} \mathrm{PEC} \xrightarrow{-\mathrm{CO_2}} \mathrm{PEO} \qquad (5)$$

Physical Chemistry Chemical Physics Accepted Manuscript

The reaction is catalyzed by the Lewis-acid PF_5 resulting from decomposition of the electrolyte salt. Residual water can also lead to the hydrolysis of $LiPF_6$.[16,39,40]

$$LiPF_6 \leftrightarrow LiF + PF_5 \quad (6)$$

$$PF_5 + H_2O \longrightarrow POF_3 + 2HF \quad (7)$$

$$POF_3 + 2x\,Li^+ + 2xe^- \longrightarrow Li_xPF_{3-x}O + x\,LiF \quad (8)$$

The decomposition products can be related to the three signals of the F 1s spectrum: The peaks at 687.7 eV, 686.4 eV and 684.1 eV are attributed to $Li_xPF_{3-x}O$ species, LiF, and additional metal fluorides such as MnF_2 and NiF_2, respectively. The latter can be formed by reaction of LNMO with HF.[14,16,41]

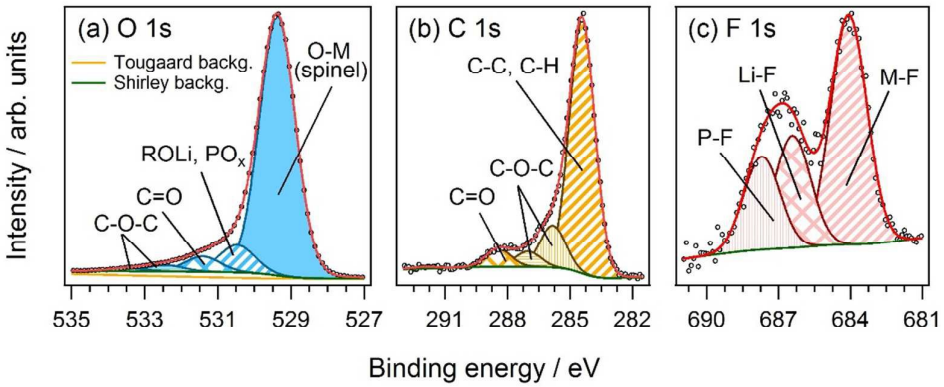

Figure 5. HAXPES (a) O 1s, (b) C 1s and (c) F 1s spectra of the LTO coated LNMO thin-film cathode with signal deconvolution and assignment to the indicated chemical species. The spectra were taken with a photon energy of 3 keV. In case of the O 1s spectrum, both the Shirley background and a Tougaard background are shown (see the text for further details).

The chemical composition of the surface layer is in line with previously reported data of similar cathode systems.[35,36,42] Edström et al. provided an overview of the cathode-electrolyte interface composition of the commonly used cathode materials $LiMn_2O_4$, $LiCoO_2$, $LiNiO_2$ and $LiNi_{1-x}Co_xO_2$ as determined by photoelectron spectroscopy.[36] These investigations revealed the presence of similar surface species as found here, including polycarbonates, polymeric hydrocarbons and electrolyte salt decomposition products such as LiF or $Li_xPO_yF_z$.

The thickness of the surface layer is calculated to be 2.9 ± 0.4 nm using Equation 3 and estimating typical errors in the relative intensities of 10 %[43] and in the IMPFs of 20 %[33] (for details see Section 2.3). This result is in good agreement with previously published ToF-SIMS data.[25] In contrast,

Physical Chemistry Chemical Physics Accepted Manuscript

formation of considerably thicker SEI layers has been reported for uncoated LNMO cathodes which had been in direct contact to the battery electrolyte. Edström et al. discussed the surface layer in terms of a solid *permeable* interface (SPI) that does not passivate the cathode surface, but enables further electrolyte degradation as fresh electrolyte can be transported continuously to the cathode surface.[15,36] This resulted in an increase of the surface layer thickness with increasing cycling number. The comparatively small thickness of the surface layer found here is in accordance to the electrochemical experiments discussed in Section 3.1, which showed an improved stability over time for the LTO coated sample.

3.4. Composition of the bulk coating

The coating material mostly consists of Ni(II), Mn(IV) and Ti(IV) oxide species. This is revealed by the analysis of the core level spectra of these elements that will be discussed in detail in Section 3.5. The bulk coating composition $Ti_xNi_yMn_zO_4$, as determined on the basis of the relative peak intensities, in dependence on the probing depth is plotted in Figure 6. The electrode composition is uniform within the margins of error, only the concentration of manganese decreases slightly but significantly. This effect can be attributed to additional MnF_2 deposited at the surface as indicated in the F 1s spectra. The bulk composition is strongly affected by the applied background correction method. For example, using a Tougaard background increases the amount of manganese by over 60 %. This result emphasizes the influence of the inelastic background intensity as the Tougaard and Shirley method define and exclude this intensity differently (see Figure 5a and Figure 8a-c). The mean bulk composition is $Li_{1.1}Ni_{0.24\pm0.03}Mn_{0.40\pm0.04}Ti_{1.2\pm0.2}O_4$, as was estimated by averaging over the probing depths and background methods. The lithium content was determined on the basis of charge neutrality considerations.

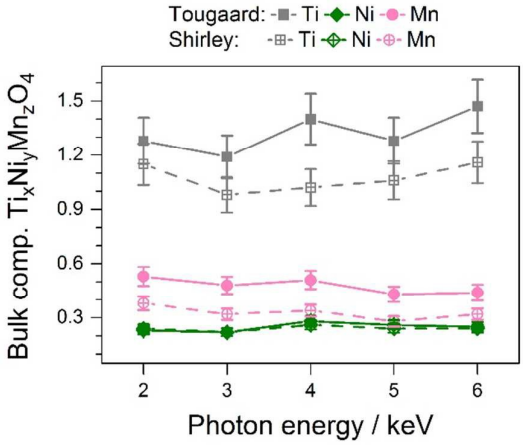

Figure 6. Dependence of the bulk coating composition $Ti_xNi_yMn_zO_4$ on the photon energy. The bulk composition is given as the relation of the relative intensities of the transition metals to the relative

Physical Chemistry Chemical Physics Accepted Manuscript

intensity of the O 1s metal oxide signal. The relative intensities were determined by using either a Shirley or a Tougaard background.

To explain the presence of Ni and Mn within the probed layer, it is proposed that nickel and manganese ions diffuse from the LNMO cathode material into the LTO lattice during the heat treatment, which is part of the preparation procedure of the electrode (see Section 2.1). Since both, LNMO and LTO crystallize in a spinel structure with similar lattice parameters[44] and similar ion radii[45], it is likely that the bulk coating can be considered as a solid solution of the two spinels LNMO and LTO. In fact, quaternary and ternary spinels of the composition $\mathrm{LiNi_{0.5}Mn_{1.5-x}Ti_xO_4}$ $(0 \leq x \leq 1.5)$ (LNMTO) and $\mathrm{Li_4Mn_{5-x}Ti_xO_{12}}$ $(0 \leq x \leq 5)$ have been reported in the literature.[46] In the quaternary spinel LNMTO, all cations except lithium prefer octahedral coordination: The cations Ni^{2+} (d^8) and Mn^{4+} (d^3) experience a high crystal field stabilization energy. Ti^{4+} (d^0) benefits from an improved Coulomb attraction at the octahedral sites.[46] In a spinel structure, the metal ions occupy the two octahedral sites (*O*) and one of the four tetrahedral sites (*T*). In case of the 4-5-12 system $\mathrm{Li_4Ti_5O_{12}}$, the cations are distributed as $\mathrm{Li_T[Li_{1/3}Ti_{2/3}]_OO_4}$. Applying this cation distribution with respect to the preferred coordination to the estimated bulk formula yields $\mathrm{Li_T[Li_{0.1}Ni_{0.24}Mn_{0.40}Ti_{1.2}]_OO_4}$. The occupation of the octahedral sites thus nearly reaches the ideal value of 2, which underlines the validity of the estimated bulk composition and the formation of a quaternary spinel solid solution. The partial replacement of Ti^{4+} (d^0) ions at the octahedral sites with the open-shell Ni^{2+} (d^8) and Mn^{4+} (d^3) ions should significantly increase the electronic conductivity of the LTO layer, as was found in previous impedance spectroscopy measurements.[25]

3.5. Analysis of the transition metal core level spectra

Figure 7 displays 2p core level spectra of titanium, nickel and manganese with the respective signal deconvolutions. Generally, oxide species forming the bulk coating material and/or fluoride species resulting from dissolution processes with hydrofluoric acid can be present in the spectra.

The Ti 2p spectrum (Figure 7a) consists of the spin-orbit split $2p_{3/2}$ and $2p_{1/2}$ main photoelectron line, two well resolved shake-up peaks and an additional broad feature, which can be attributed to an inelastic energy loss peak.[47] The origin of the two shake-up satellites can be explained in terms of exciton formation.[48] The spectrum was fitted empirically by applying a single fitting function to each of the five spectral features.

The Ti $2p_{3/2}$ BE of 457.8 eV is at the lower energy side of 16 reviewed BEs of TiO_2[49] with a mean value of 458.7 eV and a standard deviation of 1.3 eV. This quite low BE excludes the presence of large amounts of titanium fluoride species, for which $2p_{3/2}$ BEs of 461.6 eV (TiF_4) and 459.9 eV (TiF_3) were reported.[47]

Physical Chemistry Chemical Physics Accepted Manuscript

Further insight into the chemical state of titanium is provided by the energy separation ΔE_{sat} between the main $2p_{3/2}$ peak and the shake-up satellites. It has been found that ΔE_{sat} increases with the electronegativity of the ligand and the oxidation state of the metal.[50] The ΔE_{sat} values of 13.3 eV and 18.7 eV for the first and second shake-up satellite, respectively, of the Ti 2p spectrum fit well to the literature values of 13.1 eV and 18.9 eV for TiO_2.[51] For comparison, the ΔE_{sat} value of the first shake-up satellite is reported to be 14.1 eV for TiF_4 and 12.2 eV for TiF_3.[50] Thus, the chemical state of Ti corresponds to a Ti(IV) oxide similar to TiO_2 and can be attributed to the LTO coating material.

The Ni 2p spectrum (Figure 7b) displays a complex peak shape composed of various overlapping spectral features, which are divided into contributions of the $2p_{3/2}$ and $2p_{1/2}$ signals. The $2p_{3/2}$ signal exhibits two pronounced features, a main photoelectron line at 854.7 eV and a broad satellite peak at 861.0 eV. They are assigned to a $\underline{c}d^9\underline{L}$ screened and to a $\underline{c}d^8$ unscreened final-state configuration[52,53], respectively ($\underline{c}$ is a core hole, $\underline{L}$ is a ligand hole) in terms of the charge transfer model.[54]

Although these two features exist in the 2p spectra of many nickel compounds, their energy separation ΔE_{sat} has not been used for chemical state identifications in the literature (unlike in the case of Ti 2p, as was discussed above). The reason for this is that Ni 2p spectra are strongly affected by ligand-metal screening effects.[55–57] As a result, the spectral shape of these two features can vary distinctly by changing the chemical environment of the nickel atom.[57] For example, the $2p_{3/2}$ main photoelectron line of NiO exhibits a peak splitting into two components at 854.1 eV and 856.2 eV,[58] which is missing for the Ni $2p_{3/2}$ signal in Figure 7b. The occurrence of peak splitting makes a chemical state identification by investigating the energy separation between these features difficult as it becomes uncertain which peak maxima have to be chosen for the comparison. Therefore, the predominant chemical state of Ni was determined by comparing the entire spectral shape with reference spectra from the literature.

Based on the considerations at the beginning of Section 3.5, the nickel species present here should be either NiF_2 or an oxide. However, NiF_2 as the predominant species can be excluded by comparing the peak shapes and the BEs of the two $2p_{3/2}$ main features that occur at significantly higher binding energies of 858.1 eV and 863.6 eV for NiF_2[57] than those found here (854.7 eV and 861.0 eV). In contrast, the Ni 2p spectrum displayed here strongly resembles literature spectra of mixed crystals of $Ni_xMg_{1-x}O$[56,59] with high magnesium content. The similarities include both the spectral shape and the binding energies of the $2p_{3/2}$ main features. It has been shown that diluting NiO by diamagnetic Mg^{2+} ions induces a change in the Ni 2p peak shape letting the high energy shoulder of the $2p_{3/2}$ main photoelectron line of NiO vanish.[55,56] A diffusion of Ni ions into the LTO layer with diamagnetic Ti(IV) d^0 ions could induce a similar effect with respect to Ni. Thus, the chemical state of nickel should correspond to Ni ions in a (diluted) Ni(II) oxide. However, the presence of additional NiF_2 traces

Physical Chemistry Chemical Physics Accepted Manuscript

cannot be excluded, because the $2p_{3/2}$ signal was fitted with *empirically* modified fitting parameters for NiO from the literature.[52]

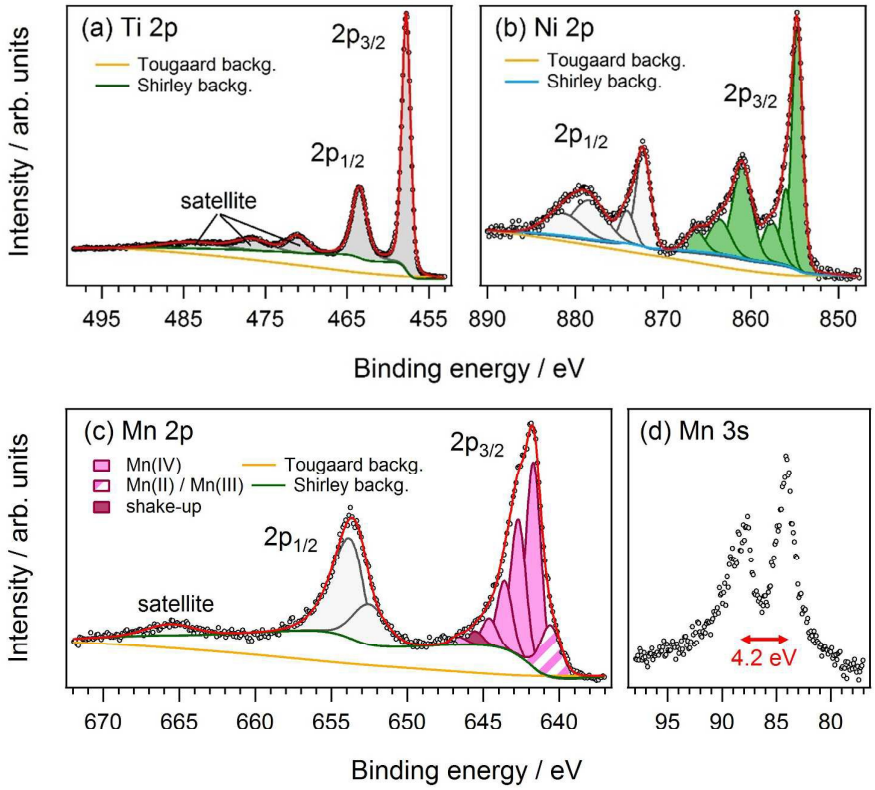

Figure 7. HAXPES core-level spectra in the regions of (a) Ti 2p, (b) Ni 2p, (c) Mn 2p and (d) Mn 3s, for the LTO coated LNMO thin-film cathode, taken with a photon energy of 3 keV. Besides the Shirley background used for the curve fitting a Tougaard background is presented in (a)-(c).

The Mn 2p spectrum (Figure 7c) consists of the well separated $2p_{3/2}$ and $2p_{1/2}$ photoelectron lines and an additional satellite at the high binding energy side. The asymmetric peak broadening observed in the $2p_{3/2}$ signal to higher binding energies and in the $2p_{1/2}$ to lower binding energies results from multiplet splitting. Mn(II), Mn(III) and Mn(IV) compounds exhibit pronounced multiplet splitting because their d-electrons can couple with the unpaired electron in the core hole. This distinct peak broadening and the complex signal shapes usually obscure the differences in the $2p_{3/2}$ binding energies of different manganese compounds. Thus, absolute binding energy values are a poor indicator for determining the chemical state of manganese.[30,60] However, the spectral shape of the Mn 2p spectra is strongly dependent on the oxidation state and the electronic configuration of the Mn atoms, according to the literature.[61] The chemical environment has only little influence, which means that different compounds can lead to similar peak shapes if the oxidation state and the

Physical Chemistry Chemical Physics Accepted Manuscript

electronic configuration of the Mn ions are the same. For example, MnF_2 and MnO display similar 2p spectra as in both cases Mn has the oxidation state +II and a high-spin d^5 electron configuration.[30,62]

The predominant oxidation state of Mn can be determined by the energy separation ΔE_{sat} of the $2p_{1/2}$ peak and the satellite signal and additionally by the multiplet splitting of the Mn 3s core level (Figure 7d).[63] The ΔE_{sat} value of 11.7 eV and the Mn 3s multiplett splitting of 4.2 eV agree well with literature data of Mn(IV)O_2 (11.8 eV and 4.4 eV, respectively).[63] For comparison, the ΔE_{sat} value and the Mn 3s multiplet splitting of Mn(III)$_2O_3$ are reported to be 10.1 eV and 5.4 eV, respectively.[64] The +II oxidation state of Mn can be excluded, because its characteristic shake-up satellite between the $2p_{1/2}$ and $2p_{3/2}$ components at about 647 eV is missing in the spectrum in Figure 7c.[30,60] Thus, the predominant chemical state of Mn corresponds to a Mn(IV) oxide. The presence of the fluoride species MnF_4 can be excluded, because it is not stable under the experimental conditions.[65]

The high binding energy side of the $2p_{3/2}$ signal can be described by a fitting model for MnO_2 based on the Gupta and Sen multiplet structure.[61] The multiplet envelope was modeled by five fitting functions with fixed relative intensities and binding energies. An additional peak assigned to a shake-up feature was added at about 645 eV according to literature.[61] The shoulder at the low binding energy side of the $2p_{3/2}$ signal that cannot be described by the fitting model is attributed to additional Mn(III) or Mn(II) species. It is known that Mn(III) contaminations are typically present in Mn(IV) oxide species.[30,61] Mn(II) could occur as MnF_2 that is formed by reaction of LNMO with HF as discussed above.

3.6. Structure of the electrode

A schematic representation of the structure of the LTO-coated LNMO thin-film cathode is shown in Figure 8. The idealized large-scale ToF-SIMS depth profile on the left hand side was reported previously.[25] The data showed the existence of two different layers assigned to LNMO and the LTO coating on top of the gold substrate. The dimension of these two layers can only be approximated as they are not clearly separated from each other. Mn and Ni species were found in the LTO coating, indicating a cross-diffusion of these ions from the LNMO layer into the LTO layer.

The right hand side of Figure 8 shows the detailed near-surface depth profile as was derived from HAXPES in the present work. The maximum probing depth is about 20 nm. Within this range, the coating film of the cathode consists of a mostly uniform mixture of Li(I), Ti(IV), Ni(II) and Mn(IV) oxides with the composition $\mathrm{Li}_{1.1}\mathrm{Ni}_{0.24\pm0.03}\mathrm{Mn}_{0.40\pm0.04}\,\mathrm{Ti}_{1.2\pm0.2}\mathrm{O}_4$. Thus, all metal ions are in the same oxidation state as in LNMO and LTO, respectively. The components of the coating possibly adopt a spinel structure by forming a solid solution of the LTO and LNMO phases with Li, Mn, Ni and Ti cations mixing on the spinel octahedral sites. The cathode is covered by a 3 nm thin surface layer

Physical Chemistry Chemical Physics Accepted Manuscript

resulting from electrolyte decomposition products. The surface layer consists predominantly of organic polymers (90 %) as well as metal fluorides and fluorophosphates (10 %).

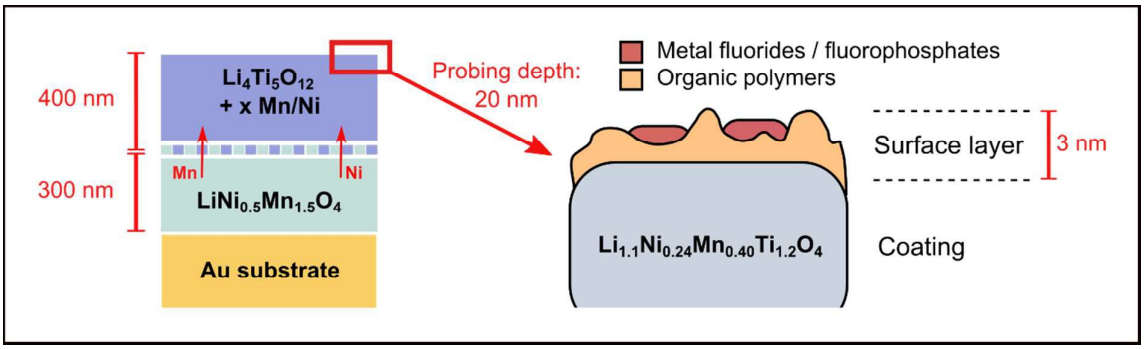

Figure 8. Depth profiles of the LTO coated LNMO thin-film cathode. Left, idealized large-scale depth profile on the basis of ToF-SIMS data.[25] Right, detailed near-surface depth profile as derived from HAXPES: Ni and Mn ions diffuse from the LNMO layer into the LTO coating during preparation of the electrode. The cathode is covered by a thin surface layer consisting of decomposition products of the electrolyte.

4. Summary and Conclusions

In this study we investigated a thin-film $LiNi_{0.5}Mn_{1.5}O_4$ cathode coated with $Li_4Ti_5O_{12}$ using electrochemical charge and discharge experiments and subsequent Hard X-ray Photoelectron Spectroscopy (HAXPES) measurements in an energy range of 2 – 6 keV. We obtained non-destructive depth profiles of the cathode in its discharged state with probing depths ranging from 6 to 20 nm. The LTO coating was found to be covered by a 3 nm thin surface layer that consists predominantly of organic polymers (90 %), as well as metal fluorides and fluorophosphates (10 %). A positive influence of the $Li_4Ti_5O_{12}$ coating on the capacity retention was found, but the size and stability of the surface layer should be further investigated. Within the probing depth, the coating itself consisted of a uniform mixture of Li(I), Ti(IV), Ni(II) and Mn(IV) oxides and had the composition $Li_{1.1}Ni_{0.24}Mn_{0.40}Ti_{1.2}O_4$ with all metal cations having the same oxidation state as in LNMO and LTO. The presence of Mn and Ni in the near-surface region indicates that these elements diffuse from the $LiNi_{0.5}Mn_{1.5}O_4$ (LMNO) layer into the $Li_4Ti_5O_{12}$ (LTO) coating. Since both LMNO and LTO are spinels, the resulting solid solution most likely also has a spinel structure. The doping of $Li_4Ti_5O_{12}$ with the open d-shell ions Ni^{2+} (d^8) and Mn^{4+} (d^3) should increase the electronic conductivity of the coating significantly and thus provides an explanation for the very low impedance of the coating material found by previous studies. Further insight into the chemical nature of the transition metal ions was achieved by analysis of the complex Ti 2p, Ni 2p and Mn 2p photoelectron spectra. Because of various processes that can accompany the primary photoemission, including shake-up or plasmon

Physical Chemistry Chemical Physics Accepted Manuscript

loss structures and multiplet splitting, binding energies of single peak maxima are often not characteristic and should not be used alone to determine the chemical state of transition metals.

Acknowledgments

Technical and financial support by the Helmholtz Zentrum Berlin für Materialien und Energie (BESSY-II) is gratefully acknowledged. H.Z. thanks the Chinese Scholarship Council (CSC) for a PhD fellowship.

Physical Chemistry Chemical Physics Accepted Manuscript

References

1 K. Kobayashi, *Nucl. Instruments Methods Phys. Res. Sect. A Accel. Spectrometers, Detect. Assoc. Equip.*, 2009, **601**, 32–47.

2 L. Kövér, *J. Electron Spectros. Relat. Phenomena*, 2010, **178-179**, 241–257.

3 S. Malmgren, H. Rensmo, T. Gustafsson, M. Gorgoi and K. Edström, in *ECS Transactions*, The Electrochemical Society, 2010, vol. 25, pp. 201–210.

4 B. Philippe, R. Dedryvère, J. Allouche, F. Lindgren, M. Gorgoi, H. Rensmo, D. Gonbeau and K. Edström, *Chem. Mater.*, 2012, **24**, 1107–1115.

5 R. Younesi, S. Urbonaite, K. Edström and M. Hahlin, *J. Phys. Chem. C*, 2012, **116**, 20673–20680.

6 S. Malmgren, K. Ciosek, M. Hahlin, T. Gustafsson, M. Gorgoi, H. Rensmo and K. Edström, *Electrochim. Acta*, 2013, **97**, 23–32.

7 K. Ciosek Högström, S. Malmgren, M. Hahlin, H. Rensmo, F. Thebault, P. Johansson and K. Edström, *J. Phys. Chem. C*, 2013, **117**, 23476–23486.

8 K. Edström, M. Herstedt and D. P. Abraham, *J. Power Sources*, 2006, **153**, 380–384.

9 P. Verma, P. Maire and P. Novak, *Electrochim. Acta*, 2010, **55**, 6332–6341.

10 K. M. Shaju and P. G. Bruce, *Dalt. Trans.*, 2008, 5471–5.

11 M. Gellert, K. I. Gries, J. Zakel, A. Ott, S. Spannenberger, C. Yada, F. Rosciano, K. Volz and B. Roling, *Electrochim. Acta*, 2014, **133**, 146–152.

12 A. Höweling, S. Glatthaar, D. Nötzel and J. R. Binder, *J. Power Sources*, 2015, **274**, 1267–1275.

13 J. W. Kim, D. H. Kim, D. Y. Oh, H. Lee, J. H. Kim, J. H. Lee and Y. S. Jung, *J. Power Sources*, 2015, **274**, 1254–1262.

14 J.-H. Kim, N. P. W. Pieczonka, Z. Li, Y. Wu, S. Harris and B. R. Powell, *Electrochim. Acta*, 2013, **90**, 556–562.

15 N. S. Norberg, S. F. Lux and R. Kostecki, *Electrochem. commun.*, 2013, **34**, 29–32.

Physical Chemistry Chemical Physics Accepted Manuscript

16 N. P. W. Pieczonka, Z. Liu, P. Lu, K. L. Olson, J. Moote, B. R. Powell and J. Kim, *J. Phys. Chem. C*, 2013, **117**, 15947–15957.

17 C. Yada, A. Ohmori, K. Ide, H. Yamasaki, T. Kato, T. Saito, F. Sagane and Y. Iriyama, *Adv. Energy Mater.*, 2014, **4**, 1–5.

18 X. Hao and B. M. Bartlett, *J. Electrochem. Soc.*, 2013, **160**, A3162–A3170.

19 G. Alva, C. Kim, T. Yi, J. B. Cook, L. Xu, G. M. Nolis and J. Cabana, *J. Phys. Chem. C*, 2014, **118**, 10596–10605.

20 Y. Y. Huang, X. L. Zeng, C. Zhou, P. Wu and D. G. Tong, *J. Mater. Sci.*, 2012, **48**, 625–635.

21 J. Li, L. Baggetto, S. K. Martha, G. M. Veith, J. Nanda, C. Liang and N. J. Dudney, *Adv. Energy Mater.*, 2013, **3**, 1275–1278.

22 X. Li, J. Liu, X. Meng, Y. Tang, M. N. Banis, J. Yang, Y. Hu, R. Li, M. Cai and X. Sun, *J. Power Sources*, 2014, **247**, 57–69.

23 T. F. Yi, J. Shu, Y. R. Zhu, A. N. Zhou and R. S. Zhu, *Electrochem. commun.*, 2009, **11**, 91–94.

24 Y.-R. Zhu, T.-F. Yi, R.-S. Zhu and A.-N. Zhou, *Ceram. Int.*, 2012, **39**, 3087–3094.

25 M. Gellert, K. I. Gries, J. Zakel, S. Kranz, S. Bradler, E. Hornberger, S. Muller, C. Yada, F. Rosciano, K. Volz and B. Roling, *J. Electrochem. Soc.*, 2015, **162**, A754–A759.

26 F. Schaefers, M. Mertin and M. Gorgoi, *Rev. Sci. Instrum.*, 2007, **78**, 123102.

27 M. Gorgoi, S. Svensson, F. Schäfers, G. Öhrwall, M. Mertin, P. Bressler, O. Karis, H. Siegbahn, a. Sandell, H. Rensmo, W. Doherty, C. Jung, W. Braun and W. Eberhardt, *Nucl. Instruments Methods Phys. Res. Sect. A Accel. Spectrometers, Detect. Assoc. Equip.*, 2009, **601**, 48–53.

28 M. Gorgoi, *HIKE Web Info 2012*, https://www.helmholtz-berlin.de accessed 15th January 2015.

29 M. Schmid, H.-P. Steinrück and J. M. Gottfried, *Surf. Interface Anal.*, 2014, **46**, 505–511.

30 M. C. Biesinger, B. P. Payne, A. P. Grosvenor, L. W. M. Lau, A. R. Gerson and R. S. C. Smart, *Appl. Surf. Sci.*, 2011, **257**, 2717–2730.

31 G. G. Fuentes, E. Elizalde, F. Yubero and J. M. Sanz, *Surf. Interface Anal.*, 2002, **33**, 230–237.

Physical Chemistry Chemical Physics Accepted Manuscript

32 J. H. Scofield, *Lawrence Livermore Lab. Rep. No. UCRL-51326*, 1973.

33 C. J. Powell and A. Jablonski, *NIST Electron Inelastic-Mean-Free-Path Database - Version 2.0*, National Institute of Standards and Technology, Gaithersburg, MD, 2010.

34 S. Tougaard, *Surf. Sci.*, 1989, **216**, 343–360.

35 J. C. Arrebola, Á. Caballero, L. Hernán, M. Melero, J. Morales and E. R. Castellón, *J. Power Sources*, 2006, **162**, 606–613.

36 K. Edström, T. Gustafsson and J. O. Thomas, *Electrochim. Acta*, 2004, **50**, 397–403.

37 P. Louette, F. Bodino and J.-J. Pireaux, *Surf. Sci. Spectra*, 2005, **12**, 59.

38 L. Yang, B. Ravdel and B. L. Lucht, *Electrochem. Solid-State Lett.*, 2010, **13**, A95–A97.

39 D. Aurbach, *J. Electrochem. Soc.*, 1996, **143**, 3809.

40 D. H. Jang, *J. Electrochem. Soc.*, 1997, **144**, 3342.

41 N. P. W. Pieczonka, L. Yang, M. P. Balogh, B. R. Powell, K. Chemelewski, A. Manthiram, S. a Krachkovskiy, G. R. Goward, M. Liu and J. H. Kim, *J. Phys. Chem. C*, 2013, **117**, 22603–22612.

42 L. Baggetto, R. R. Unocic, N. J. Dudney and G. M. Veith, *J. Power Sources*, 2012, **211**, 108–118.

43 C. Battistoni, G. Mattogno and E. Paparazzo, *Surf. Interface Anal.*, 1985, **7**, 117–121.

44 P. Villars and K. Cenzual, *Pearson's Crystal Data - Crystal Structure Database for Inorganic Compounds (on CD-ROM)*, ASM International, Ohio, 2014.

45 R. D. Shannon, *Acta Crystallogr. Sect. A*, 1976, 32, 751–767.

46 M.-L.-P. Le, P. Strobel, C. V. Colin, T. Pagnier and F. Alloin, *J. Phys. Chem. Solids*, 2011, **72**, 124–135.

47 C. Mousty-Desbuquoit, J. Riga and J. J. Verbist, *Inorg. Chem.*, 1987, **26**, 1212–1217.

48 D. K. G. de Boer, C. Haas and G. A. Sawatzky, *Phys. Rev. B*, 1984, **29**, 4401–4419.

Physical Chemistry Chemical Physics Accepted Manuscript

49 J. T. Mayer, U. Diebold, T. E. Madey and E. Garfunkel, *J. Electron Spectros. Relat. Phenomena*, 1995, **73**, 1–11.

50 C. Mousty-Desbuquoit, J. Riga and J. J. Verbist, *Inorg. Chem.*, 1987, **26**, 1212–1217.

51 M. Oku, K. Wagatsuma and S. Kohiki, *Phys. Chem. Chem. Phys.*, 1999, **1**, 5327–5331.

52 A. P. Grosvenor, M. C. Biesinger, R. S. C. Smart and N. S. McIntyre, *Surf. Sci.*, 2006, **600**, 1771–1779.

53 A. F. Carley, S. D. Jackson, J. N. O'Shea and M. W. Roberts, *Surf. Sci.*, 1999, **440**, L868–L874.

54 P. S. Bagus, E. S. Ilton and C. J. Nelin, *Surf. Sci. Rep.*, 2013, **68**, 273–304.

55 M. A. Van Veenendaal and G. A. Sawatzky, *Phys. Rev. Lett.*, 1993, **70**, 2459–2462.

56 M. Atanasov and D. Reinen, *J. Electron Spectros. Relat. Phenomena*, 1997, **86**, 185–199.

57 M. C. Biesinger, L. W. M. Lau, A. R. Gerson and R. S. C. Smart, *Phys. Chem. Chem. Phys.*, 2012, **14**, 2434.

58 A. N. Mansour, *Surf. Sci. Spectra*, 1994, **3**, 231.

59 M. Oku and K. Hirokawa, *J. Electron Spectros. Relat. Phenomena*, 1977, 10, 103–110.

60 M. Oku, K. Hirokawa and S. Ikeda, *J. Electron Spectros. Relat. Phenomena*, 1975, **7**, 465–473.

61 H. W. Nesbitt and D. Banerjee, *Am. Mineral.*, 1998, **83**, 305–315.

62 S. P. Kowalczyk, L. Ley, F. R. McFeely and D. a. Shirley, *Phys. Rev. B*, 1975, **11**, 1721–1727.

63 M. A. Stranick, *Surf. Sci. Spectra*, 1999, **6**, 31.

64 M. A. Stranick, *Surf. Sci. Spectra*, 1999, **6**, 39.

65 N. Wiberg, A. F. Holleman and E. Wiberg, *Lehrbuch der Anorganischen Chemie*, Walter de Gruyter & Co., Berlin, 102. edn., 2007.

Physical Chemistry Chemical Physics Accepted Manuscript